Surfaces and Interfaces 36 (2023) 102507

Contents lists available at ScienceDirect

Surfaces and Interfaces

journal homepage: www.sciencedirect.com/journal/surfaces-and-interfaces

Tuning layer thickness and layer arrangement in a $GdMnO_3$ and $GdMnO_3$-$MoSe_2$ bi-layer absorber to cover the S, C, and X band frequency range

Dengwu Wang [a,*], Cuihong Zhang [a], Achmad Jusuf Zulfikar [b], Sadok Mehrez [c,d], Isabelle Huynen [e,*], Ibrahim Mahariq [f], Ibrahim Elbadawy [f]

[a] Xi'an Key Laboratory of Advanced Photo-electronics Materials and Energy Conversion Device, School of Information Engineering, Xijing University, Xi'an, 710123, China
[b] Excellent Centre of Innovations and New Science, Universitas Medan Area, Medan, Indonesia
[c] Department of Mechanical Engineering, College of Engineering at Al Kharj, Prince Sattam bin Abdulaziz University, 11942, Saudi Arabia
[d] Department of Mechanical Engineering, University of Tunis El Manar, ENIT, BP 37, Le Belvédère, 1002 Tunis, Tunisia
[e] Université catholique de Louvain, ICTEAM Institute, Place du Levant 3, Louvain-la-Neuve B-1348, Belgium
[f] College of Engineering and Technology, American University of the Middle East, Kuwait

ARTICLE INFO

Keywords:
Bi-layer absorber
$GdMnO_3$
$MoSe_2$
Absorption performance
Single layer

ABSTRACT

The bi-layer absorber's microwave absorption performance can be enhanced by adjusting and manipulating the layers' composition, layer thickness, and layer arrangement. Herein, two magnetic and magneto-electric components, $GdMnO_3$ (G) and $GdMnO_3$-50 wt.% $MoSe_2$ (GM), were prepared via a solvothermal method. In particular, the impact of filler loading and layer thickness on microwave absorption characteristics was examined. The findings indicate that a single-layer absorber sample containing G or GM components independently did not have good microwave absorption capability. On the other hand, a bi-layer absorber sample with G as the matching layer (1.5 mm thickness) and GM as the absorber (0.5 mm thickness) possesses exceptional -44 dB reflection loss with 9 GHz of effective absorption bandwidth, which covers S, C, and almost the whole X band frequency range. The optimal 3D network architecture of the G particles' rod-like morphology, which improves the impedance matching property, may be to blame for this phenomenon. Additionally, this special 3D network architecture gives an abundance of interfaces to disperse electromagnetic waves in addition to many channels for microwave reflecting and scattering. More crucially, the composites' microwave absorption mechanism is investigated and studied, which offers a trustworthy guide for making a bi-layer absorber.

1. Introduction

As electromagnetic interferences can have a detrimental effect on human health and the operation of electronic devices [1], efficient solutions are necessary to reduce these effects. Among these, microwave absorbers have been developed for military as well as civilian applications in order to make a target invisible to radar signals. Well-known applications of radar cross section (RCS) reduction include stealth military bombers and the prevention of parasitic reflections induced by mast and rotating blades of wind turbines. For more than two decades microwave absorbing materials (MAM) are developed based on a polymer dielectric matrix containing conductive inclusions and aiming to absorb the signal through ohmic dissipation of the incident power [2–6] in order to reduce reflection and/or convert electromagnetic energy to radiation for healthcare multifunctional sensing applications [7]. An overview of techniques developed for the design and fabrication of MAM can be found in [8–12]. A MAM layer coating a metallic target allows for reducing the radar cross-section (RCS) to make the target invisible to the radar signal (Salisbury configuration).

As conductive charges are used in MAM for the attenuation of the signal, they may be responsible for reflection. To avoid this, magnetic particles can be added to the composite MAM [13–16] in order to lower the impedance at the input interface as close as possible to that of air. In [17] a MAM based on Samarium doped Cobalt nano ferrite is produced by sol-gel auto combustion. The ferrite material is used as a substrate supporting a fractal metamaterial pattern. The metamaterial-based

* Corresponding authors.
E-mail addresses: farmouse403@163.com (D. Wang), isabelle.huynen@uclouvain.be (I. Huynen).

https://doi.org/10.1016/j.surfin.2022.102507
Received 15 September 2022; Received in revised form 9 October 2022; Accepted 21 November 2022
Available online 30 November 2022

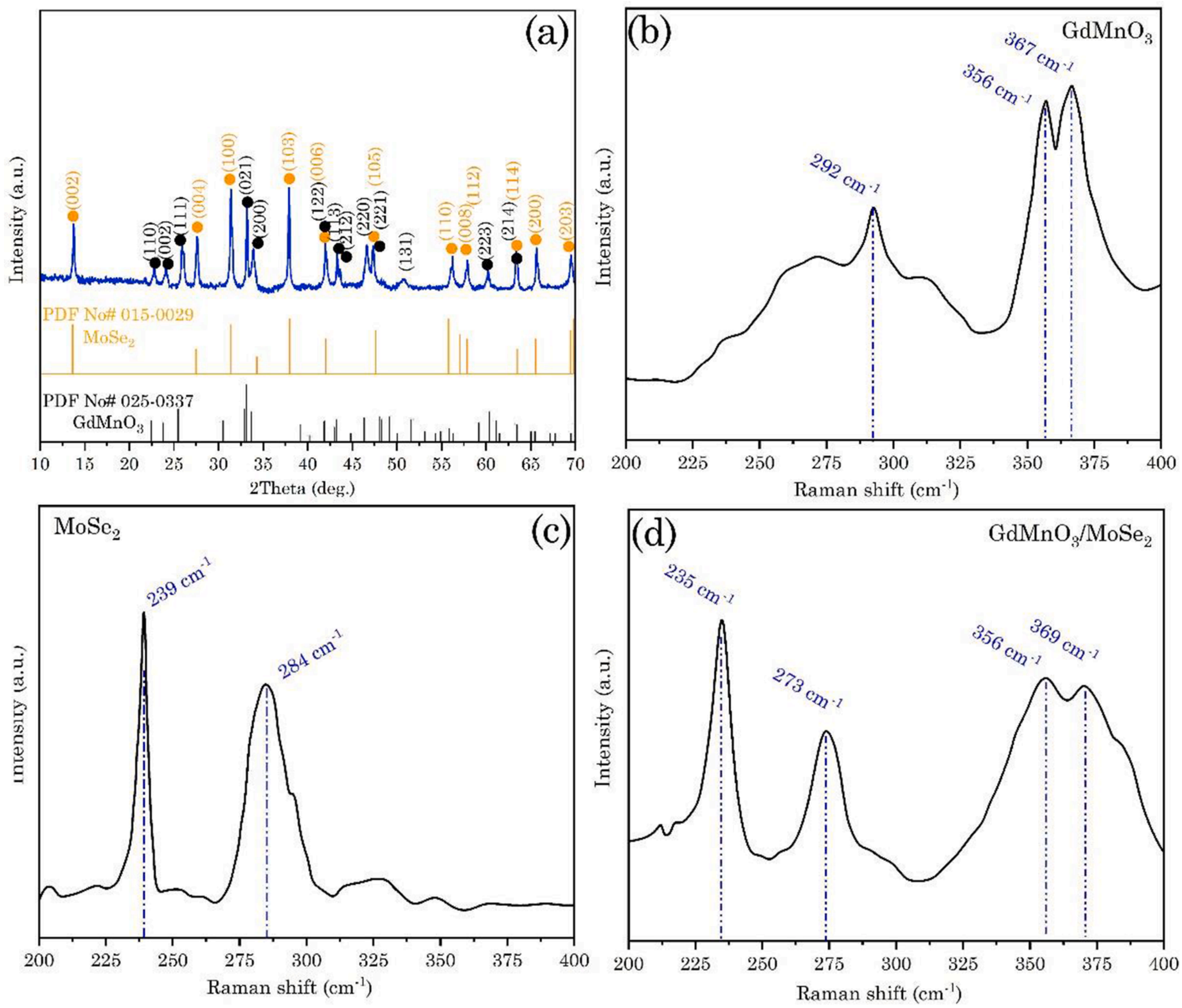

Fig. 1. a) XRD, b,c) Raman spectra analysis results of as-prepared powders.

MAM is simulated using measured electromagnetic parameters of the ferrite, and multiple peaks of narrow absorption are predicted in the 1-6 GHz frequency range for both TE and TM polarization modes. In [18] the same authors prepare a bismuth-doped Cobalt–Zinc ferrite material using again sol-gel auto combustion technique, to achieve shielding efficiency (SE). A simulated total SE value of 12 dB is obtained from 8 to 14 GHz, while shielding due to absorption is only 4 dB, meaning that shielding is induced by reflection rather than by absorption. Using again the same synthesis technique in [19], the authors prepare Ba-doped Co–Zn ferrite, and claim 12.8 d B for total SE, while shielding due to absorption is again around 4 dB, inducing a similar conclusion. Similarly, the sol-gel method is used in [20] for the synthesis of Copper-doped Cobalt–Zinc Ferrite nanoparticles, and in [21] for the synthesis of Pr and Cobalt-doped BiFeO3 multiferroics nanomaterials; in this last work the same approach as in [17] is applied and peaks of absorption are observed at multiple frequencies for the simulated metamaterial structure in the 1 – 6 GHz frequency range.

A particular family of magnetic charges is manganese oxide (MnO_3). In [22] $La_{0.7}Sr_{0.3}MnO_3$ powder was synthesized using the sol-gel method and anchored by hydrothermal method on reduced graphene oxide, before and dispersion into paraffin with 70% concentration. The resulting composite slab shows a reflectivity of -47.9 dB around 10.7 GHz for a thickness of 2.5 mm and over an effective 10 dB bandwidth of 3 GHz. In [23], a sol-gel method was used for preparing LaCaSr-MnO_3 material, which shows moderate return losses of only 4 dB, around 10.44 GHz. In [24], a nanocrystalline $La_{0.7}Sr_{0.3}MnO_3$ sample was prepared by a combination of the solid-state reaction and high-energy ball milling methods, then mixed with paraffin. Best performances are obtained around 14.8 GHz for a thickness of 2 mm; the return loss observed is 25 d B, for an effective bandwidth of 1 GHz. Finally, in [25] carbonyl iron /$La_{0.6}Sr_{0.4}MnO_3$ composites were prepared by the sol-gel method. The best return loss of 12 dB is obtained at 10.5 GHz for a thickness of 0.8 mm, and the corresponding absorption bandwidth is 2.5 GHz.

For comparison, works based on nonmagnetic materials are also reported. In [26], carbon-nanotube/silica composite powders were produced by ultrasound. At room temperature, the composite having 10 wt.% exhibits a return loss of -19 d B for a thickness of 2 mm, and the effective absorption bandwidth is 4.2 GHz around 10 GHz. And in [27] a sol-gel method was used to prepare carbon fiber silicate composites. The minimal return loss of -10.4 d B is obtained around 9.5 GHz for a thickness of 5 mm, but with a negligible effective absorption bandwidth.

Manganese oxide MnO3 nanowires prepared by thermal decomposition exhibit a return loss of – 21 dB at 10 GHz and an effective absorption bandwidth of 13 GHz for a thickness of 2 mm [28]. When combined with gadolinium (Gd) to form $GdMnO_3$, manganese oxide is reported to have dielectric as well as magnetic properties and is reported as multiferroic ceramics [29]. $GdMnO_3$ is a strongly correlated electron system, and its electric and magnetic properties are closely related to the electron structure and vacancy defects features.

In this work, we investigate the microwave absorption capability of $GdMnO_3$ powder (G) prepared by the solvothermal method and its

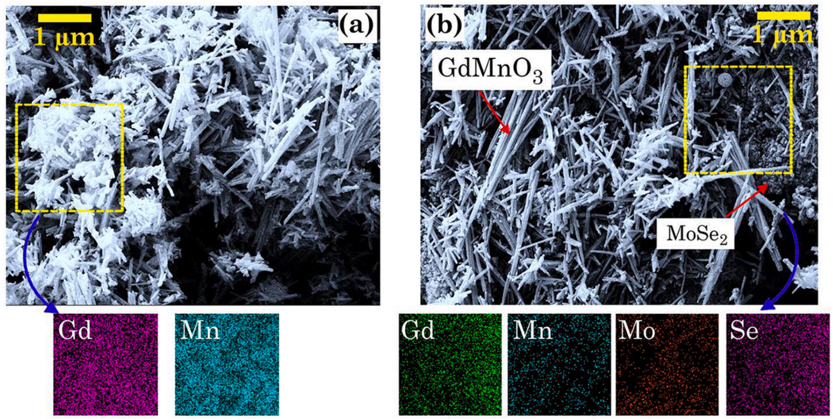

Fig. 2. FESEM images and elemental mapping analysis of a) G and b) GM samples.

combination with MoSe2 in order to form a GdMnO3-50 wt.% MoSe2 composite powder (GM). Section 2 of the paper presents the experimental synthesis and measurement protocols, while Section 3 discusses Physico-chemical and morphology properties of G and GM products, as well as their microwave performances including absorption. Finally, conclusions are presented in Section 4.

2. Materials and methods

2.1. Preparation of $GdMnO_3$ particles via solvothermal method (G)

A stoichiometric amount of gadolinium(III) nitrate and manganese (II) acetate were added to the ethylene glycol as solvent and stirred continuously magnetically for one hour. The obtained metal complex solution was mixed for one hour before urea was added. Urea had a mole ratio that was three times greater than the total amount of metal ions'. The aforementioned suspension was put into a PTFE (poly-tetrafluoroethylene) cup, kept for 15 hours at 220°C in an electric oven, and then left to cool to room temperature. To produce powder, the product was sintered at 900°C for two hours after being rinsed with the mixture of ethanol and water.

2.2. Preparation of $GdMnO_3$-50 wt.% $MoSe_2$ composite powder (GM)

As-prepared GdMnO3 particles with rod-like morphology were combined with distilled water and stirred for an hour. Two distinct solutions were made by dissolving the selenium powder and sodium molybdate dihydrate in hydrazine hydrate and distilled water, respectively. The total weight of the $MoSe_2$ procedure was determined to be 50% of the weight of the $GdMnO_3$ powder. Two prepared solutions were additionally added to the $GdMnO_3$ suspension and stirred for an additional hour. After that, the completed mixture was heated at 200°C for 24 hours in a PTFE cup. The centrifuged powder was washed to remove any impurities and then dried and sintered for an hour at 800°C.

2.3. Instrumental characterization

The structural characters of synthesized powders were revealed via X-ray diffraction (XRD, PANalytical) and Raman spectroscopy (Renishaw). Field emission scanning electron microscopy (FESEM, Sigma VP) was utilized to analyze the morphological aspects. The electromagnetic characteristics of the single layer absorber samples in the 2-18 GHz frequency range were assessed using a vector network analyzer (model PNA-N5244A, AGILENT).

2.4. Fabrication of absorber samples

The proper weights (35 and 50 wt.%) of each powder were first weighted, mixed thoroughly with melted paraffin, and then shaped into a cylindrical ring form with a 2 mm thickness for the manufacture of single-layer absorber samples (G35, G50, GM35, and GM50). Then, measurements on a vector network analyzer in the frequency range of 2-18 GHz were made using the transmission line theory. Based on the results of the single layer absorber, the absorption performance of double-layer absorbers was simulated.

3. Results and discussion

3.1. Physico-chemical analysis

In the two-theta range of 10-70°, the powders' XRD patterns and Raman spectra were captured. The $MoSe_2$ phase was confirmed to have formed by the XRD investigations, which revealed the presence of diffraction crystallographic planes (002), (004), (100), (103), (006), (105), (110), (008), (112), (114), (200), and (203) for the $MoSe_2$ phase, which completely matched with JPCDS card# 015-0029. Additionally, other indexed peaks matching with the 025-0337 JPCDS card no. correspond to the $GdMnO_3$ crystal planes (110), (002), (111), (021), (200), (122), (113), (212), (220), (221), (131), (223) and (214). The effective synthesis of the $GdMnO_3/MoSe_2$ nanocomposite is evident from this. No additional diffraction peak was seen, indicating its phase purity. Regarding the Raman spectra results, $GdMnO_3$ has a perovskite structure, as is well known. Thus, the stretching, bending, and tilt vibration modes of the MnO_6 octahedron, which are clearly seen in Fig 1b. The aforementioned modes are responsible for the peaks at 292, 356, and 367 cm^{-1}, respectively. In-plane and out-of-plane bending vibrations are attributed to two vibrational modes in Raman spectroscopy of $MoSe_2$. These 239 and 284 cm^{-1} peaks are due to in-plane and out-of-plane bending vibration, respectively (Fig. 1c).

With the help of a $MoSe_2$ layer, this approach was successful in characterizing the surface functionalization of $GdMnO_3$. There are four peaks seen in Fig. 1d, two of which correspond to the bending and tilt vibrations of the Mo-Se bond at 235 and 273 cm^{-1} and the Mn-O bond at 356 and 369 cm^{-1} (uncoated part), respectively (Fig. 1d). In Fig. 1d) all peaks shift to lower values and the peaks of 292 and 284 cm^{-1} are overlapped and observed at 273 cm^{-1}.

3.2. Morphological analysis

The morphological characteristics of the prepared G and GM samples are shown in Fig. 2(a,b). The rod-like structure for $GdMnO_3$ samples is revealed by the FE-SEM data. It is unmistakably evident that the $MoSe_2$

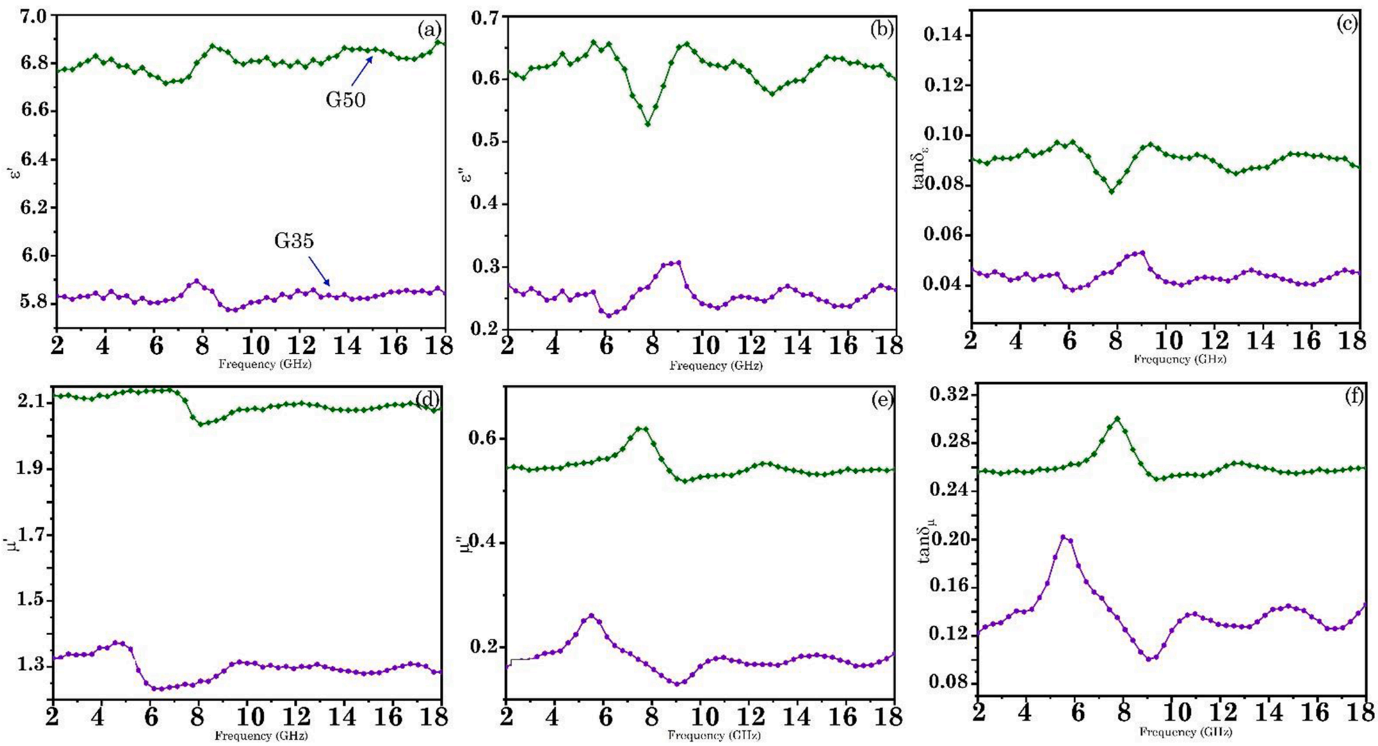

Fig. 3. Electromagnetic parameters for G samples as a function of the concentration in the 2 -18 GHz range: a) real part of permittivity, b) imaginary part of permittivity, c) tan δ_ε, d) real part of permeability, e) imaginary part of permeability, f) tan δ_μ.

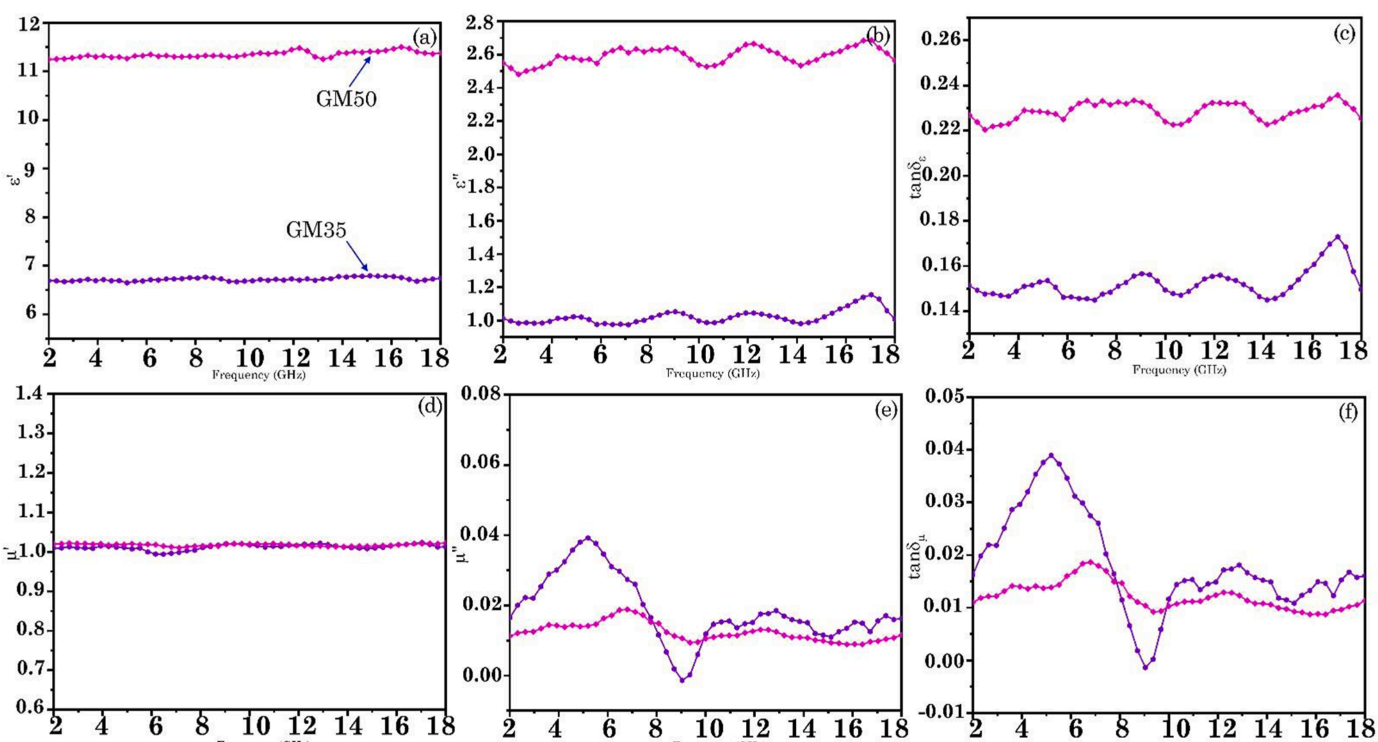

Fig. 4. Electromagnetic parameters of GM samples in the 2 -18 GHz range: a) real part of permittivity, b) imaginary part of permittivity, c) tan δ_ε, d) real part of permeability, e) imaginary part of permeability, f) tan δ_μ of GM samples in 2-18 GHz.

particle morphology is sphere-like with a diameter ranging from 40 to 50 nm and the G particle morphology is rod-like with a length in the range of 2-3 μm. The photos show that the components have been thoroughly blended because there are lots of sphere and rod particles present. The creation of rod-like particles in the G sample is caused by the spontaneous assembly of adjacent particles, which is made easier by the presence of EG and urea as surfactants in the synthesis process. Additionally, the elemental mapping results clearly show that Gd, Mn,

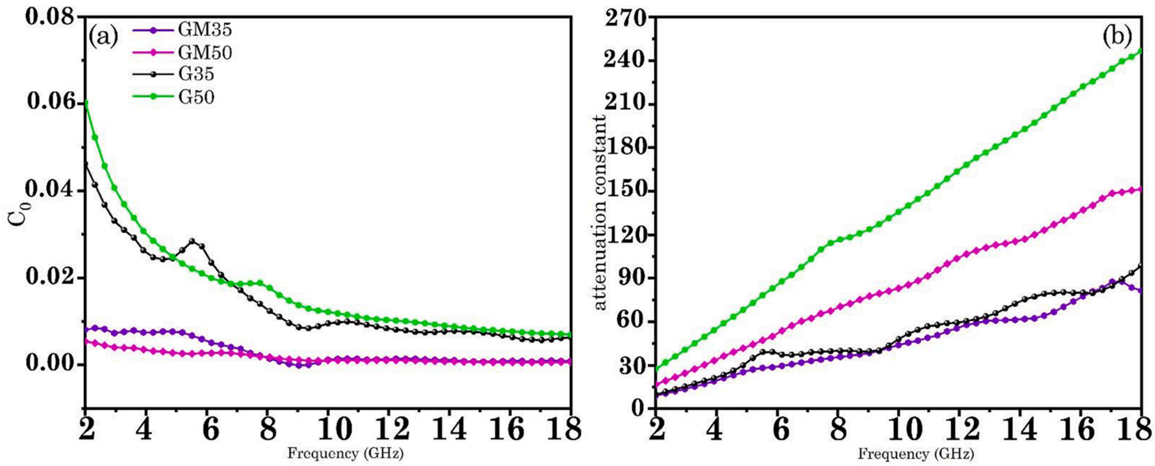

Fig. 5. a) The C_0 - f curves and b) The attenuation constant (α), of samples.

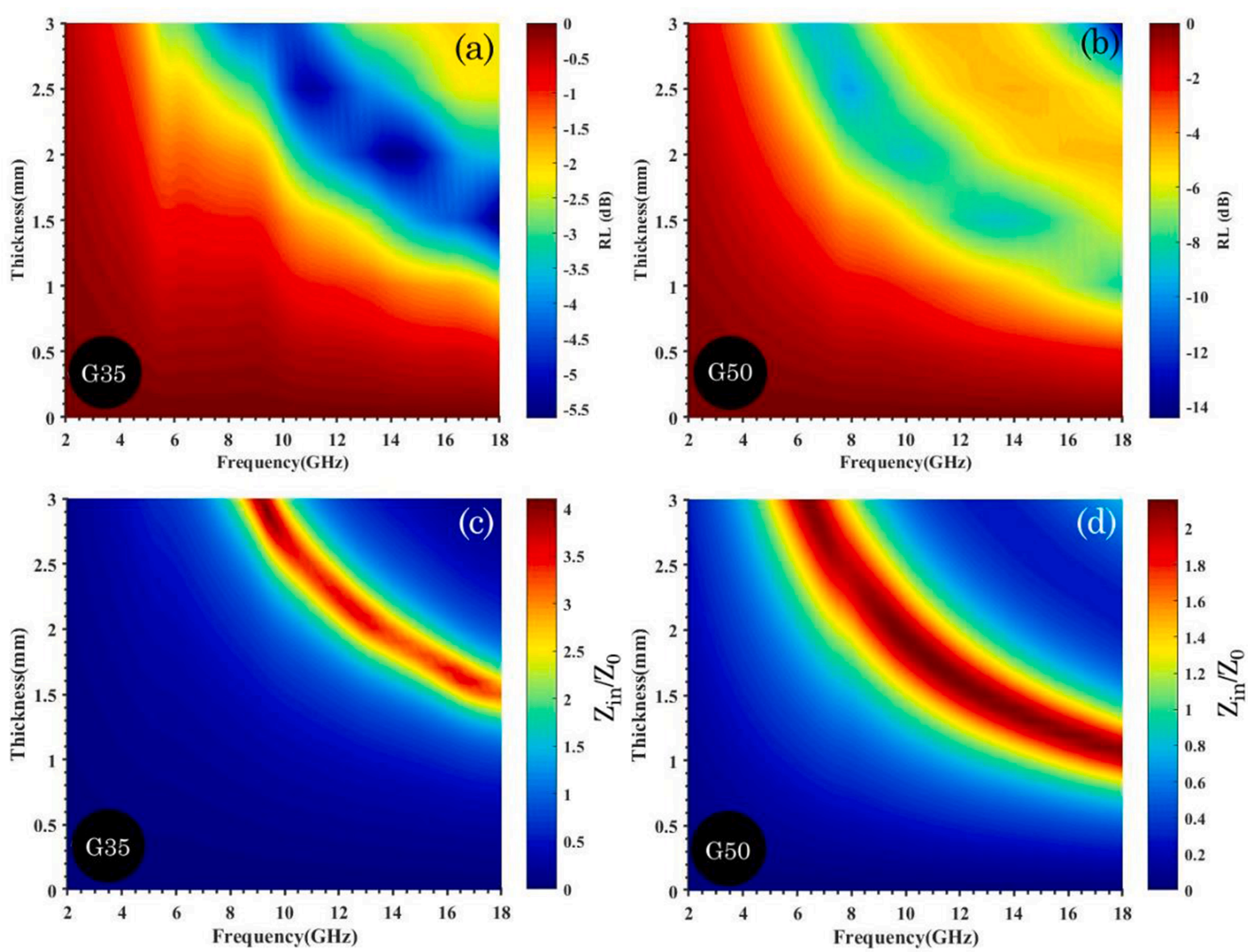

Fig. 6. a,b) RL contour map and a-d) Z_{in}/Z_0 contour map and of G composite samples.

Mo, and Se elements are present in the nanocomposite and are distributed uniformly throughout.

3.3. Electromagnetic (EM) properties of samples

The EM properties of the samples prepared and measured according to Section 2.4 are presented in Figs. 3 and 4.

Fig. 3 shows EM parameters for samples G versus frequency, and

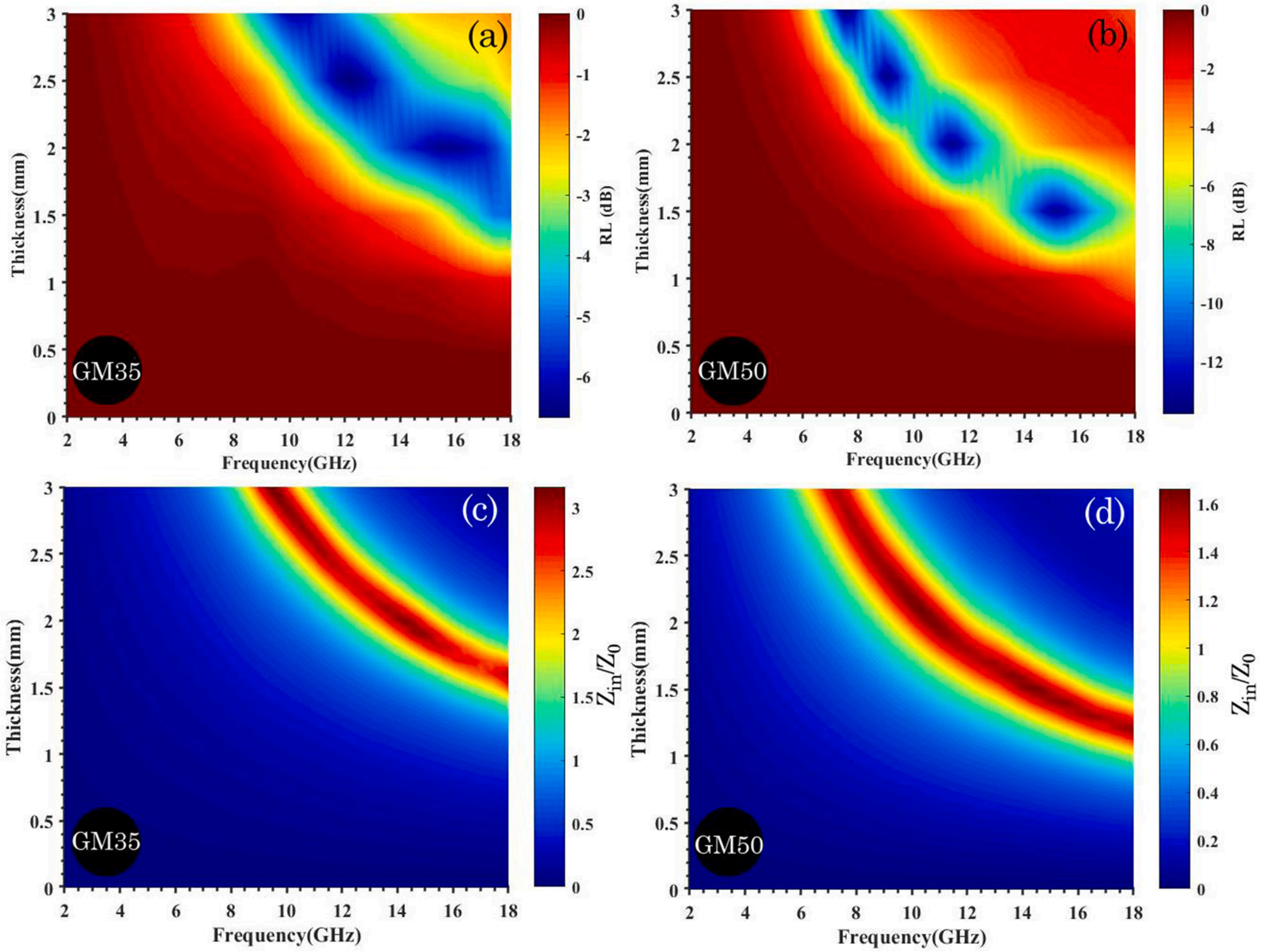

Fig. 7. a,b) RL contour map and a-d) Z_{in}/Z_0 contour map and of GM composite samples.

depending on the concentration. The dielectric parameters ε', ε" and $\tan\delta_\varepsilon$ shown in the top row of the figure drastically increase with the concentration. This observation is in accordance with the behavior of a two-phase composite medium, combining G and paraffin. Increasing the content in G enhances its contribution to the dielectric parameters of the composite. More noticeable, the magnetic parameters shown at the bottom row of the figure are significantly higher than unity, confirming that G samples have a significant magnetic behavior.

Fig. 4 reveals that the behavior of the GM samples is significantly different since dielectric parameters are higher than for G samples, especially the dielectric losses, which are roughly multiplied by 2. The magnetic parameters shown in the bottom row of the figure show no significant variation with the concentration, and their value is almost equal to that of air, i.e. μ' close to 1 and μ" close to zero, fluctuations being attributed to noise artifacts on low measured values. This means that GM samples have no significant magnetic behavior. A possible explanation is the high content (50%) of MoSe2 which is not magnetic and dilutes the magnetic content of the composite while its interaction with magnetic $GdMnO_3$ particles reduces the magnetization of the GdMnO3-50 wt.% MoSe2 composite powder. As well the high content of MoSe2 which is metallic modifies the conductivity of the composite powder, resulting in an increase of both real and imaginary parts of the permittivity.

From the comparison of results of Figs. 3 and 4, we can conclude that the GM sample having high losses is adequate for attenuating the signal, while G material having a permeability greater than one will favor the penetration of the signal in the absorber, thus reducing its reflection, hence also favoring its absorption. The combination of these properties is applied to the absorption mechanism of bilayer configuration discussed in Section 3.5.

Fig. 5 analyzes two other parameters influencing microwave absorption in G and GM samples. The eddy current loss factor noted C_o is given by expression (1) and plotted in Fig. 5a; for the two GM samples, the obtained value is zero. This is in accordance with the fact that these samples show no magnetic behavior so that μ' and μ" involved in (1) and shown in Fig. 4 are equal to zero. The C_o behavior of the 2 G samples having parameters depicted in Fig. 3 tends to be constant at high frequency, allowing us to affirm the presence of magnetic losses due to eddy currents [30].

$$C_0 = \mu''\mu'^{-2}f^{-1} = 2\pi\mu_0\sigma d^2 \tag{1}$$

The attenuation coefficient α is given by expression (2) and shown in Fig. 5b:

$$\alpha = \frac{2\pi}{c}\sqrt{2\mu'\varepsilon'}\sqrt{\frac{\mu''\varepsilon''}{\mu'\varepsilon'} - 1 + \sqrt{\left(\frac{\mu''}{\mu'}\right)^2 + \left(\frac{\varepsilon''}{\varepsilon'}\right)^2 + \left(\frac{\mu''\varepsilon''}{\mu'\varepsilon'}\right)^2 + 1}} \tag{2}$$

For each sample, G or GM, the attenuation constant α involves the parameters ε', ε", μ', μ" given in Fig. 3 or 4 respectively. Similarly the attenuation constant increases with concentration for both G and GM samples, and GM50 shows higher attenuation than G50, most probably

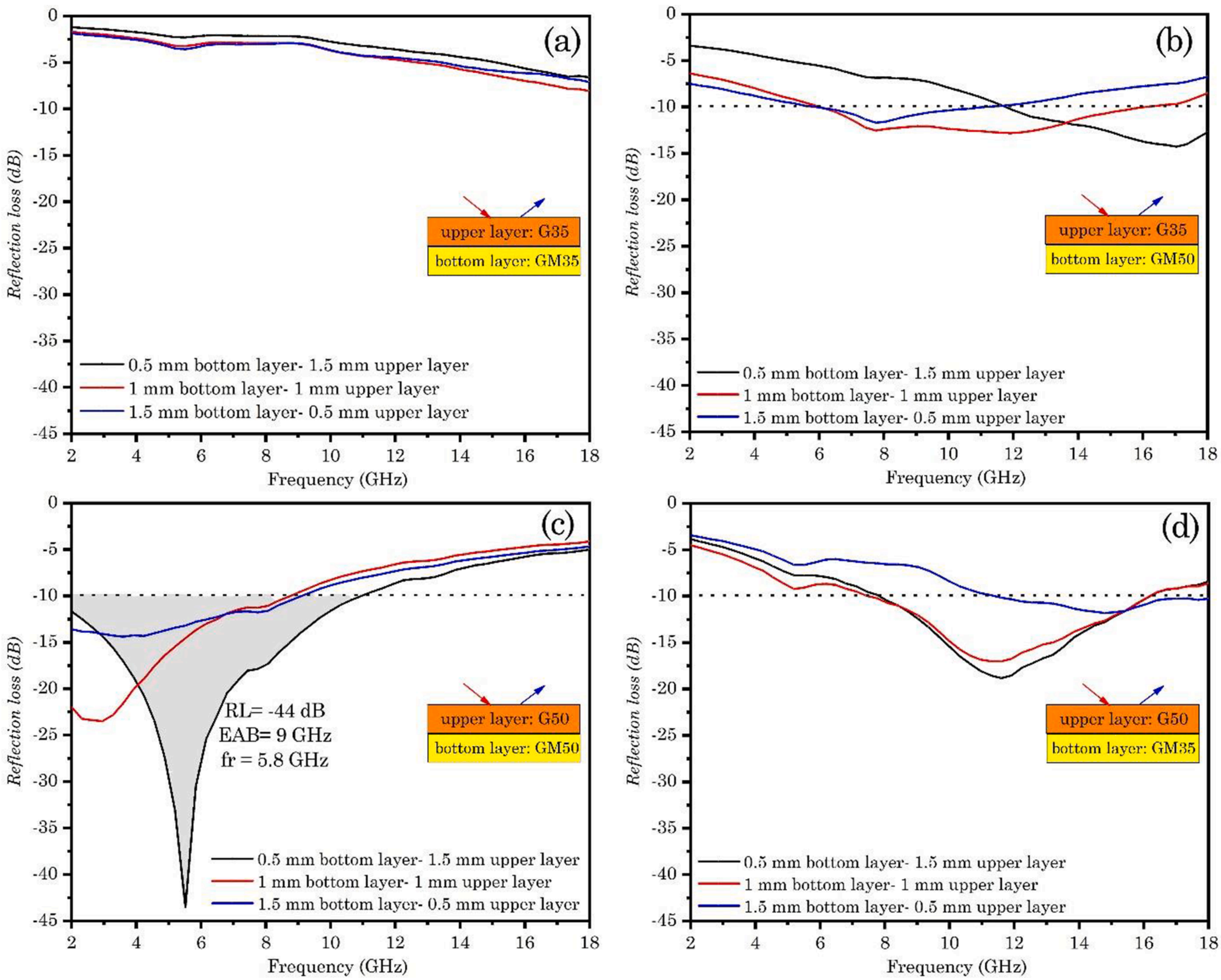

Fig. 8. RL curves of the double-layer absorber in which G is placed at the top layer and GM placed at the bottom layer with a total thickness of 2 mm.

Table 1
Performances of bilayer absorbers versus state-of-the art.

Sample	Thickness (top/ bottom)	f_o (GHz)	RL (dB)	EAB (GHz)	FB (%)	FOM
G35/ GM50	0.5 mm / 1.5 mm	7	11	5	71	786
	1 mm / 1 mm	10	12	10	100	1200
	1.5 mm / 0.5 mm	17	13	7	41	535
G50/ GM50	0.5 mm / 1.5 mm	3	14	6	200	2800
	1 mm / 1 mm	3	23	6	200	4600
	1.5 mm / 0.5 mm	**5.5**	**44**	**9**	**164**	**7200**
G50/ GM35	0.5 mm / 1.5 mm	15.5	11	7	45	497
	1 mm / 1 mm	11	15	8	73	1091
	1.5 mm / 0.5 mm	11	17	8	73	1236
[16]	**2.5**	**10.7**	**47.9**	**3**	**28**	**1343**
[18]	2	14.33	25	1	7	174
[19]	0.8	10.5	12	2.5	24	286
[26]	2	10	19.2	4.2	42	806
[27]	5	9.5	10.4	/	/	/
[28]	**2**	**10**	**21**	**13**	**130**	**2730**

due to the higher dielectric losses of GM samples.

3.4. Microwave absorption performances of the single layer configuration

The microwave absorption capability of our samples can be evaluated using a reflective configuration when each considered sample is backed with a metallic plate. In this configuration, the microwave signal entering the sample is attenuated/absorbed twice, firstly when traveling towards the metallic plate, and secondly when traveling back towards the input of the sample, after its reflection by the metallic plate. If the absorption through the sample is efficient, almost all the signal is absorbed during its propagation in the sample, so that no reflection is detected at the input of the sample. The reflection at the input of a sample backed by a metallic plate is noted as R and has the following expression, depending on the input impedance Z_{in} [31]:

$$R = \left(\frac{Z_{in} - Z_O}{Z_{in} + Z_O}\right) \quad (3)$$

Where

$$Z_{in} = \sqrt{\frac{\mu}{\varepsilon}}\, Z_o\, tanh(\gamma\ d\ ) \quad (4)$$

and

$$\gamma = j\,2\,\pi\,f\,\sqrt{\varepsilon\,(\,1 - j\,\tan\delta_{\varepsilon})\,\mu\,\left(1 - j\,tan\delta_{\mu}\right)}\Big/c_{O} \tag{5}$$

The reflection R is usually expressed in dB in order to represent reflection loss RL:

$$RL = 20\,log_{10}\left(\frac{Z_{in} - Z_{O}}{Z_{in} + Z_{O}}\right) \tag{6}$$

In (4-5) Z_o is the 377 Ω, frequency assigned with f, C_0 as the speed of light, d is the layer's thickness and electromagnetic parameters such as permittivity (ε), permeability (μ), and loss tangents ($\tan\delta_{\varepsilon}$ and tand δ_{μ}). From (3,6) RL is minimum when Z_{in} approaches 0. A good absorber usually achieves RL < - 10 dB.

Fig. 6 shows the 2D plots of RL (top, a,c) and $|Z_{in}|$ (bottom, b,d) for the 35% (left) and 50% (right) concentration of the D samples, as a function of thickness d and frequency f. The 35% concentration fails to meet the – 10 dB criterion. The situation is quite similar for the 50% concentration, since only a narrow region around d = 3 mm and f = 18 GHz shows R around – 10 dB.

Fig. 7 shows similar 2D plots for the GM samples. Again the 35% concentration fails to reach RL < - 10 dB for all thicknesses, while for 50% concentration the - 10 dB threshold can be reached for frequencies superior to 7 GHz and thicknesses superior to 1.3 mm.

3.5. Microwave absorption performances of bilayer configuration

Since the single-layer configurations do not allow to achieve good absorption performances, this section investigates the performances of bilayer configurations.

Four cases are considered in Fig. 8 in all cases, the top layer is made of G material and the bottom layer of GM material. Indeed the G material shows a significant magnetic content with permeability higher than unity, and this favors the input matching [12-15/13-16] by increasing the impedance $\sqrt{\frac{\mu}{\varepsilon}}$ involved in (4) in order to approach the 377 Ω of air. Placing the G material as the top layer makes the penetration of the signal in the sample easier and favors its absorption. Four combinations of stacking are investigated: G35/GM35 in figure a), G35/GM50 in figure b), G50/GM50 in figure c), and G50/GM35 in figure d). Also 3 different combinations of thicknesses are considered for each top / bottom stack: 1.5 mm / 0.5 mm, 1 mm / 1 mm, and 0.5 mm / 1 mm.

It is clear from Fig. 8 that the best performances in terms of reflection losses RL and bandwidth are obtained for the stack G50/GM50 with thicknesses 1.5 mm / 0.5 mm for top and bottom layers respectively: RL min = -44 Db and the effective absorption bandwidth EAB defined as the bandwidth wherein RL < -10 dB is equal to 9 GHz. The stack G35/GM35 fails to achieve RL < - 10 dB, the stack G35/GM50 reaches at best – 13 dB, while stack G50/GM35 reaches at best – 17 dB.

Table 1 summarizes the performances of the various configurations presented in Figure 9, satisfying RL < -10 dB, and compares them with the literature.

In Table 1 the figure of merit FOM = FB x |RL| means that the highest magnitude of reflection losses |RL| over the highest possible frequency bandwidth is desired. The fractional bandwidth is defined as FB = EAB / f_o, in order to gauge the high-frequency absorption performance of the samples.

Clearly, several bilayer combinations of our samples outperform the best results from the literature, i.e. [16,28], thanks to their exceptional fractional bandwidth combined with high reflection loss.

4. Conclusions

$GdMnO_3$ (G) and $GdMnO_3$-50 wt% MoSe2 (GM), two magnetic and magnetoelectric components, were synthesized using a solvothermal approach in this study. It was specifically looked at how filler loading and layer thickness affected microwave absorption characteristics. The results show that a sample of a single-layer absorber lacking either G or GM components did not have a satisfactory microwave absorption performance. In contrast, a bi-layer absorber sample with G as the matching layer (1.5 mm thickness) and GM as the absorber (0.5 mm thickness) has a remarkable -44 dB reflection loss with 9 GHz of effective absorption bandwidth, covering S, C, and nearly the whole X band frequency range. This behavior may be caused by the rod-like morphology of the G particles' ideal 3D network design, which enhances the impedance matching property. This unique 3D network architecture also offers a large number of interfaces for scattering electromagnetic waves as well as numerous channels for microwave reflection and scattering. More importantly, the microwave absorption mechanism of the composites is explored and researched, providing a reliable manual for creating bi-layer absorbers.

CRediT authorship contribution statement

Dengwu Wang: Conceptualization, Methodology. **Cuihong Zhang:** Conceptualization, Methodology. **Achmad Jusuf Zulfikar:** Validation. **Sadok Mehrez:** Validation, Investigation, Supervision, Funding acquisition. **Isabelle Huynen:** Writing – original draft, Writing – review & editing. **Ibrahim Mahariq:** Conceptualization, Investigation, Supervision, Funding acquisition. **Ibrahim Elbadawy:** Methodology, Validation, Supervision, Funding acquisition.

Declaration of Competing Interest

None.

Data availability

Data will be made available on request.

Acknowledgements

Isabelle Huynen acknowledges the financial support of the National Fund for Scientific Research (FNRS, Belgium).

References

[1] N. Violette, Electromagnetic Compatibility Handbook, Springer, Berlin/ Heidelberg, Germany, 2013.
[2] M. Jafarian, S.F. Kashani Bozorg, A.A. Amadeh, Y. Atassi, Hierarchical brain-coral-like structure (3D) vs rod-like structure (1D): Effect on electromagnetic wave loss features of $SrFe_{12}O_{19}$ and $CoFe_2O_4$, Ceram. Int. 47 (2021) 30448–30458.
[3] Kim, J.-B. Design of Salisbury screen absorbers using dielectric lossy sheets. In Proceedings of the 2011 IEEE International Conference on Microwave Technology & Computational Electromagnetics, Beijing, China, 22–25 May 2011; pp. 1–2.
[4] M. Jafarian, S.F. Kashani Bozorg, A.A. Amadeh, Y. Atassi, Boosted microwave dissipation performance via integration of magneto/dielectric particles with hierarchical 3D morphology in bilayer absorber, J. Magn. Magn. Mater. 539 (2021), 168363.
[5] Q. Gu, M. Jafarian, S.S.S. Afghahi, Y. Atassi, R. Al-Qassar, Tuning the impedance matching characteristics of microwave absorbing paint in X-band using copper particles and polypyrrole coating, Mater. Res. Bull. 125 (2020), 110780.
[6] M. Jafarian, S.F. Kashani Bozorg, A.A. Amadeh, Y. Atassi, Nano-architectured NiO shell vs 3D microflowers morphology toward enhancement of magneto-electric loss in mesoporous magneto-electric composite, Ceram. Int. 47 (2021) .20595–.20609.
[7] Min Zhang, Mao-Sheng Cao, Jin-Cheng Shu, Wen-Qiang Cao, Lin Li, Jie Yuan, Electromagnetic absorber converting radiation for multifunction, Mater. Sci. Eng. R Rep. 145 (2021), 100627.
[8] D. Micheli, R. Pastore, A. Vricella, M. Marchetti, Matter's electromagnetic signature reproduction by graded-dielectric multilayer assembly, IEEE Trans. Microw. Theory Tech. 65 (8) (2017) 2801–2809.
[9] Pawar Shital Patangrao, High frequency millimetre wave absorbers derived from polymeric nanocomposites, Polymer 84 (2016) 398–419.
[10] Jean-Michel Thomassin, Polymer/carbon based composites as electromagnetic interference (EMI) shielding materials, Mater. Sci. Eng. R Rep. 74 (7) (2013) 211–232.
[11] Fusheng Wen, Fang Zhang, Zhongyuan Liu, Investigation on Microwave Absorption Properties for Multiwalled Carbon Nanotubes/Fe/Co/Ni Nanopowders as Lightweight Absorbers, J. Phys. Chem. C 115 (29) (2011) 14025–14030.

[12] Zhou Wang, Guang-Lin Zhao, Electromagnetic wave absorption of multi-walled carbon nanotube–epoxy composites in the R band, J. Mater. Chem. C 2 (2014) 9406–9411.

[13] P.M. Raj, D. Mishra, H. Sharma, S. Swaminathan, R. Tummala, Chap. 1 Nanomagnetic materials and structures, and their applications in integrated rf and power modules, Nanomagnetism (2014) 1–29.

[14] F. Qin, H.X. Peng, N.Y. Pankratov, M. Phan, L.V. Panina, M. Ipatov, V. Zhukova, A. Zhukov, J. Gonzalez, Exceptional electromagnetic interference shielding properties of ferromagneticmicrowires enabled polymer composites, J. Appl. Phys. 108 (2010), 044510.

[15] X. Ma, Q. Zhang, Z. Luo, X. Lin, G. Wu, A novel structure of ferroaluminum-based sandwich composite for magnetic and electromagnetic interference shielding, Mater. Des. 89 (2016) 71–77.

[16] K. Singh, A. Ohlan, A. Bakhshi, S. Dhawan, Synthesis of conducting ferromagnetic nanocomposite with improved microwave absorption properties, Mater. Chem. Phys. 119 (2010) 201–207.

[17] MN Akhtar, S Makhdoom, MA Baqir, M Yousaf, MA Khan, KM Batoo, "Enhanced structural, electromagnetic and absorption features of CoSm ferrite-metamaterial absorbers through synergistic effects", Ceram. Int. 48 (20), 29561-29571.

[18] KM Batoo, M Hadi, A Chauhan, R Verma, M Singh, OM Aldossary, "High-frequency applications of bismuth-doped Co-Zn ferrite nanoparticles for electromagnetic interference filter and multilayer inductor chip fabrication", Appl. Phys. A 128 (4), 1-17.

[19] Khalid Mujasam Batoo, Muhammad Hadi, Ritesh Verma, Ankush Chauhan, Rajesh, "Improved microwave absorption and EMI shielding properties of Ba-doped Co-Zn ferrite", Ceram. Int. 48 (3), 3328-3343.

[20] M Hadi, KM Batoo, A Chauhan, OM Aldossary, R Verma, Y Yang, " Tuning of structural, dielectric, and electronic properties of Cu doped Co-Zn ferrite nanoparticles for multilayer inductor chip applications", Magnetochemistry 7 (4), 53.

[21] MN Akhtar, M Yousaf, MA Baqir, KM Batoo, MA Khan, "Pr-Co co-doped BFO multiferroics nanomaterials for absorber applications", Ceram. Int. 47 (2), 2144-2154.

[22] Kelan Yan, Feng Yin, Chao Pang, Xiuhui Zuo, Qitu Zhang, Liming Shen, Runhua Fan and Ningzhong Bao, "Broadband microwave absorber constructed by reduced graphene oxide/La0.7Sr0.3MnO3 composites, RSC Adv. 9 (2019) 41817.

[23] R I Admi, S A Saptari, A Tjahjono, I N Rahman, W A Adi, Synthesis and characterization microwave absorber properties of La0.7(Ca1-xSrx)0.3MnO3 prepared by Sol-Gel method, J. Phys. Conf. Ser. 1816 (2021), 012091.

[24] Tran Dang Thanh, Chu Thi Anh Xuan, Ta Ngoc Bach, et al., Magnetic and microwave absorbing properties of La0.7Sr0.3MnO3 nanoparticles, AIP Advances 12 (2022), 035134.

[25] Y.L. Cheng, J.M. Dai, D.J. Wu, Y.P. Sun, Electromagnetic and microwave absorption properties of carbonyl iron/La0.6Sr0.4MnO3 composites, J. Magn. Magn. Mater. 322 (2010) 97–101.

[26] Bo Wen, Mao-Sheng Cao, et al., Temperature dependent microwave attenuation behavior for carbon-nanotube/silica composites, Carbon 65 (2013) 124–139.

[27] Mao-Sheng Cao, Wei-Li Song, Zhi-Ling Hou, Bo Wen, Jie Yuan, The effects of temperature and frequency on the dielectric properties, electromagnetic interference shielding and microwave-absorption of short carbon fiber/silica composites, CA R B O N (2010) 788–796, 4 8.

[28] Qiangchun Liu, Zhenfa Zi, Qipeng Zheng, Min Zhang, Jianming Dai, Large-Scale Synthesis, Characterization, and Microwave Absorption Properties of Manganese Oxide Nanowires, in: Proceedings of The Thirteenth China International Nanoscience and Technology Symposium (CINSTS14) Part V of V 164, 2015.

[29] Fengjiao Ye, Haiyang Dai, Manman Wang, Jing Chen, Tao Li, Zhenping Chen, The structural, dielectric, and magnetic properties of GdMnO3 multiferroic ceramics, J. Mater. Sci. Mater. Electron. 31 (2020) 3590–3597.

[30] M. Jafarian, S.S.S. Afghahi, Y. Atassi, A. Sabzi, New insights on microwave absorption characteristics of magnetodielectric powders: Effect of matrix chemical nature and loading percentage, J. Magn. Magn. Mater. 492 (2019), 165624.

[31] M. Jafarian, S.S.S. Afghahi, Y. Atassi, A. Loriamini, Promoting the microwave absorption characteristics in the X band using core-shell structures of Cu metal particles/PPy and hexaferrite/PPy, J. Magn. Magn. Mater. 493 (2020), 165680.